On three-dimensional reconstruction of a neutron/x-ray source from very few two-dimensional projections

Volegov, Petr Lvovich
Danly, Christopher R.
Merrill, Frank Edward
Simpson, Raspberry
Wilde, Carl Huerstel

On 3D reconstruction of a neutron/x-ray source from very few 2D projections

P. L. Volegov[a], C. R. Danly, F. E. Merrill, R. Simpson, C. H. Wilde

Los Alamos National Laboratory, Los Alamos, New Mexico 87544, USA

The neutron imaging system at the National Ignition Facility (NIF) is an important diagnostic tool for measuring the two-dimensional size and shape of the source of neutrons produced in the burning DT plasma during the stagnation phase of ICF implosions. Very few two-dimensional projections of neutron images are available to reconstruct the three-dimensional neutron source. In this paper we present a technique that has been developed for the 3D reconstruction of neutron and x-ray sources from a minimal number of 2D projections. We present the detailed algorithms used for this characterization and the results of reconstructed sources from experimental data collected at Omega.

Keywords: neutron imaging, National Ignition Facility, NIF, Omega, Inertial confinement fusion, ICF

---

[a] Corresponding author: volegov@lanl.gov

I. INTRODUCTION

The National Ignition Facility (NIF) performs experiments to study inertially confined thermonuclear burn of deuterium-tritium (DT) plasmas[1, 2]. Presently the required densities and pressures are achieved through indirect ablative compression of plastic (CH) capsules containing a DT ice layer surrounding DT gas. In this design, the gas inside of the DT ice layer is compressed and heated by the convergent implosion to reach temperatures of ~5 keV and the DT fuel assembly reaches an areal density, ρR, of greater than ~1 g/cm^2. With the appropriate fuel assembly conditions, this system creates a less dense but hot central region (the "hot spot"), surrounded by higher density but colder DT fuel (the "cold fuel"). Fusion reactions and the subsequent energy deposition from alpha particles within the DT fuel can further heat this hot spot, generating energy beyond what is achieved from implosive mechanical work[3]. If this system is tuned appropriately to establish ignition in the fuel assembly these implosions are predicted to release over a 10^6 joules of fusion energy and more than 10^{17} neutrons[4].

Tuning these implosions to achieve ignition requires the measurement of plasma conditions, such as symmetry, hot-spot volume and cold-fuel volume, at very small length and time scales. The hot spot is predicted to have a 30-50 µm diameter, while the surrounding cold fuel is expected to be ~100 µm in diameter, and the fusion conditions must be maintained for ~100 ps [2].

An existing neutron imaging system (NIS) at the National Ignition Facility (NIF)[5] is used to provide data on the size and shape of the fusion hotspot and the surrounding cold fuel for ICF experiments. Typical neutron emission measurements at NIF show a clear asymmetric hotspot and cold fuel. A single-view image currently measured with NIS, which is a summation of the neutrons generated along the line of sight of the instrument (90-315 in NIF polar coordinates), cannot alone provide enough information to determine the three dimensional distribution of the hotspot or cold fuel. This is unfortunate, as the source of this asymmetry is not fully understood and is possibly an indication of the processes which dominate the stagnation phase of these high convergence implosions, the most critical time in implosion performance. The collection of images obtained from several directions, i.e. multi-dimensional data, would enable the study of the effects of three dimensional asymmetries on the stagnation phase physics, providing a measurement of 3D asymmetry and performance to observe correlations between 3D structure and performance as well as guiding the development and validation of 3D models and simulations.

A conceptual design has been developed for the addition of two new neutron imaging systems at NIF[6]. However, by the nature of the current design of the existing neutron imaging system, the number of different views which can be implemented is limited. Thus very few projections are available to reconstruct the 3D source, resulting in an incomplete data set for tomographic reconstruction, which is a severely ill-posed problem[7].

To obtain a meaningful solution in the case of limited tomographic views assumptions (*a priori* knowledge) about the properties of the object need to be included to restrict the solution to the physically plausible domain. Therefore, algebraic reconstruction algorithms are more appropriate for this application because they allow for imposing additional conditions on the reconstructed solution, at a significant computational expense. It was previously stated that algebraic reconstruction techniques (such as SIRT or ART) in the case of limited number of projections have a tendency to produce less severe artifacts in limited view reconstructed objects[8]. It was further

hypothesized that regularized iterative reconstruction algorithms, for example Maximum Entropy iterative reconstruction, could result in even smaller artefacts[8], at the cost of imposing a bias on the solution. Here we use an iterative Generalized Expectation-Maximization (GEM) algorithm[9] to reconstruct three dimensional neutron or x-ray sources in the context of inertial confinement fusion experiments.

In summary the available experimental information from a few projections does not allow for reliable artifact free reconstruction of the three-dimensional source in the general case. However, as we show below for source reconstruction in ICF experiments, it is possible using an iterative Expectation Maximization (EM) algorithm to reconstruct from a few two dimensional projections, if the projections are measured along judiciously chosen directions. The reconstructed three-dimensional emission source is not free from artifacts, but with careful analysis the reconstruction preserves the main features of the underlying source.

II. THEORY/ALGORITHM

As we mentioned in the introduction, the images obtained in ICF experiments with a neutron or x-ray imaging system represent two-dimensional projections of a three-dimensional source. The distance between source and detector is much greater than the size of the source, so assuming the paraxial approximation[10], which is equivalent to parallel beam projection tomography, and neglecting attenuation of neutrons and hard x-rays by the source (consider an optically thin source), each point of these projections is a linear integral given by the following equation:

$$I(\mathbf{d}, \widehat{\mathbf{p}}) \equiv P_{\widehat{\mathbf{p}}}\{S\}(\mathbf{d}) = \int_{-\infty}^{\infty} S(\mathbf{d} + \xi\widehat{\mathbf{p}}) \, d\xi = \int_{-\infty}^{\infty} S(a\hat{\mathbf{e}}_1 + b\hat{\mathbf{e}}_2 + \xi\widehat{\mathbf{p}}) \, d\xi \tag{1}$$

Here $I(\mathbf{d}, \widehat{\mathbf{p}})$ is the intensity measured at position $\mathbf{d} \equiv a\hat{\mathbf{e}}_1 + b\hat{\mathbf{e}}_2$ on the detector for the view along direction $\widehat{\mathbf{p}}$; $\hat{\mathbf{e}}_1$ and $\hat{\mathbf{e}}_2$ are basis vectors in the detector coordinate system; $\widehat{\mathbf{p}}$ is the projection direction. The vectors $\hat{\mathbf{e}}_1$, $\hat{\mathbf{e}}_2$, and $\widehat{\mathbf{p}}$ uniquely define the view, i.e. 2D projection of the 3D object. Typically the unit vectors $\hat{\mathbf{e}}_1$, $\hat{\mathbf{e}}_2$, and $\widehat{\mathbf{p}}$ are chosen to be orthogonal.

Assuming a suitable discretization of the volume and the projections, using cube-shaped volume elements (voxels), integral equation (1) can be approximated as a system of linear equations:

$$I_{i,j,v} = \sum_k \sum_l \sum_m L_{i,j,v}^{k,l,m} s_{k,l,m} \tag{2}$$

For each view of number, v, $I_{i,j,v} \equiv I(\mathbf{d}_{i,j}, \widehat{\mathbf{p}}_v)$ is the measured value of the pixel (i,j) at position $\mathbf{d}_{i,j} = (a_i, b_j)$ on the detector for the projection direction $\widehat{\mathbf{p}}_v$; $s_{k,l,m} \equiv S(\mathbf{r}_{k,l,m})$ is the value of the source inside the voxel (k,l,m) at position $\mathbf{r}_{k,l,m} = (x_k, y_l, z_m)$; and $L_{i,j,v}^{k,l,m}$ is the length of intersection of the line through the pixel (i,j) along the direction $\widehat{\mathbf{p}}_v$ with the voxel (k,l,m) known as the Siddon coefficients[11]. The described projection geometry and the introduced notations are illustrated in Figure 1.
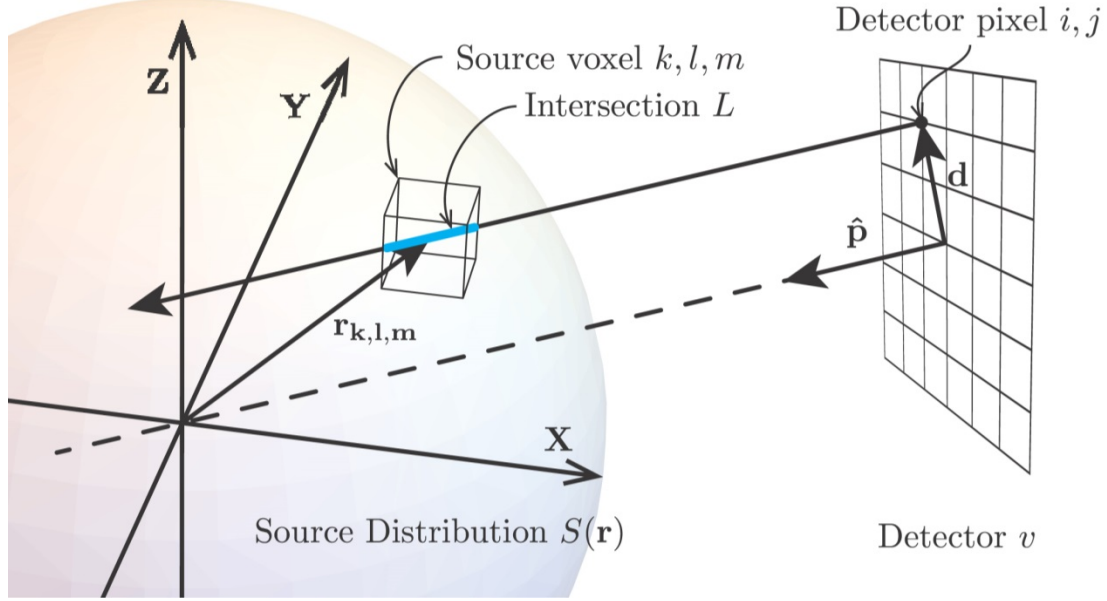
Figure 1. Projection geometry and notations

Equation (2) can be written in a matrix notation:

$$\mathbf{I} = \mathbf{L}\mathbf{s} \tag{3}$$

where $\mathbf{I} = \left[I_\zeta \equiv I_{i,j,v} \right]$, $\mathbf{L} = \left[L_{\zeta,\eta} \equiv L_{i,j,v}^{k,l,m} \right]$, and $\mathbf{s} = \left[s_\eta \equiv s_{k,l,m} \right]$. Here the composite index $\zeta = (i, j, v)$ numerates pixels in the projections, and the composite index $\eta = (k, l, m)$ numerates the voxels.

In the real world the image $\mathbf{I}$ is measured along with noise, so the neutron source reconstruction problem becomes:

$$\mathbf{I} = \mathbf{L}\mathbf{s} + \boldsymbol{\varepsilon}, \tag{4}$$

where $\mathbf{I}$ and $\mathbf{L}$ are known, and $\boldsymbol{\varepsilon}$ is unknown additive noise.

One well established method of solving equation (4) is the expectation-maximization (EM) algorithm[12], also known as the Lucy-Richardson method[13, 14]. The algorithm starts with an initial guess for the solution, calculates the projected image, and iteratively updates the solution according to Bayes' theorem for conditional probabilities. It was shown that the iterations converge to the solution in the sense of maximum-likelihood estimation (MLE)[13, 15]. An implementation of this and the similar technique is described in details in[10].

However, as it was mentioned before, in ICF experiments very few 2D projections are available to reconstruct the 3D source, thus equation (4) in practice is typically ill-defined, i.e. the number of unknowns is greater than the number of independent equations. This aspect of the problem leads to an increasingly non-smooth, and, therefore, in our application, non-physical solution as iterations approach ML solution. To overcome this property of this algorithm an additional restriction on the solution is necessary.

One way to achieve this in the framework of an EM algorithm is to introduce a probability measure of the solution based on a Gibbs distribution[9]:

$$p_G(\mathbf{S}) = \frac{1}{K} e^{-U(\mathbf{S})/\beta} \tag{5}$$

where $p_G(\mathbf{S})$ is the probability of the configuration $\mathbf{S}$, $U(\mathbf{S})$ is the "energy" function, K is a normalization constant, and β is a regularization parameter. With a Gibbs prior the solution of the equation (4) now becomes[9]:

$$\mathbf{S}_G = \arg\max_{\mathbf{S}} \left\{ l(\mathbf{S}) - \frac{U(\mathbf{S})}{\beta} \right\}, \tag{6}$$

where $l(\mathbf{S})$ is a log-likelihood function. Note that as $\beta \to +\infty$ equation (6) results in the ML estimation.

The energy function, in many cases, can be limited to pair-wise priors[16]:

$$U(\mathbf{S}) = \sum_{\eta} \sum_{\eta' \in N(\eta)} V(s_\eta, s_{\eta'}) \tag{7}$$

where $N(\eta)$ is a set of neighbor voxels of the voxel η; and $V(s_\eta, s_{\eta'})$ is a potential function defined by values of the voxels η an η'. It was shown that in most cases a first-order neighborhood in three dimensions may be sufficient[9]. Typically, the potential functions are quadratic, i.e. $V(s_\eta, s_{\eta'}) = (s_\eta - s_{\eta'})^2$, or linear, i.e. $V(s_\eta, s_{\eta'}) = |s_\eta - s_{\eta'}|$. The latter is also known as the Huber function. These potentials can be augmented by introducing the generalized Huber functions $h_{\mu,p}(t)$ [17]:

$$V(s_\eta, s_{\eta'}) = h_{\mu,p}(t) = \begin{cases} |t|^2/2\mu, & \text{if } |t| \le \mu^{1/(2-p)} \\ |t|^p/p - \delta, & \text{if } |t| > \mu^{1/(2-p)} \end{cases} \tag{8}$$

where $t = s_\eta - s_{\eta'}$; $\delta = (1/p - 1/2)\mu^{p/(2-p)}$; when $p = 0$, $|t|^p/p$ is assumed to be $\log|t|$ and $\delta = (\log\mu - 1)/2$. In the case $p = 1$ the potential function is a linear, i.e. a Huber function, and for $p = 2$ the potential is quadratic. To avoid singularities this potential is always quadratic in the small neighborhood of $t = 0$, which is defined by the parameter μ. Note that the potential is a non-convex function for $p < 1$.

The derivation and implementation of the iterative algorithm considered in this work to solve equation (6) is described in detail in[9]. The algorithm is referred to as a generalized expectation-maximization (GEM) algorithm.

Finally, it should be mentioned, that an important question for practical applications of an iterative scheme is when to stop the iterations. One simple and useful stopping rule, considered here, is to compute the relative change of the residual from one iteration to the next iteration: $\Delta\rho \equiv (\rho^{(t)} - \rho^{(t+1)})/\rho^{(t)}$, where $\rho^{(t)}$ is some measure of the residual at the t-th iteration, and stop the iterations as soon as this relative change is below some value. Typically, reduced chi-square or Kullback-Leibler distance is used as a measure of the residual. Empirically it was found that critical value $\sim 10^{-3}$ provides a robust stopping criterion in most cases.

III. MODEL RECONSTRUCTION

Typically tomographic reconstructions utilize a large number of views collected in the same plane. This is the preferable measurement scheme and, for example, the tomographic diagnostic in the radiographs of the Advanced Hydrotest Facility (AHF) project[18] settled on this scheme. It was estimated that to ensure reliable reconstruction of a

three-dimensional object minimum 12 views uniformly distributed in the equatorial plane were required. When using a smaller number of views, however, the reconstruction strategy is different and become experiment specific. To illustrate this statement and evaluate the fidelity of the reconstruction of a 3D source using very few projections (~3-5), we model three different projection schemes:

a) three equatorial views: 1 - (90, 0), 2 – (90, 60), 3 – (90, 120)

b) three views along coordinate axes: 1 - (0, 0), 2 – (90, 0), 3 – (90, 90)

c) four views "equally" distributed: 1 - (0, 0), 2 – (45, 0), 3 – (90, 60), 4 – (135, 120)

Here the numbers in parentheses are polar coordinates - (inclination, azimuth) – of the corresponding view in degrees. The model 3D source we used in the simulations to study the measurement scenarios consists of a toroid imbedded inside a sphere. The emission (of x-rays or neutrons) is set to 1 arbitrary unit (a.u.) inside the sphere and to 3 a.u. inside the toroid. Figure 2 shows the model source and angular position of the views (projections) used in the simulations.
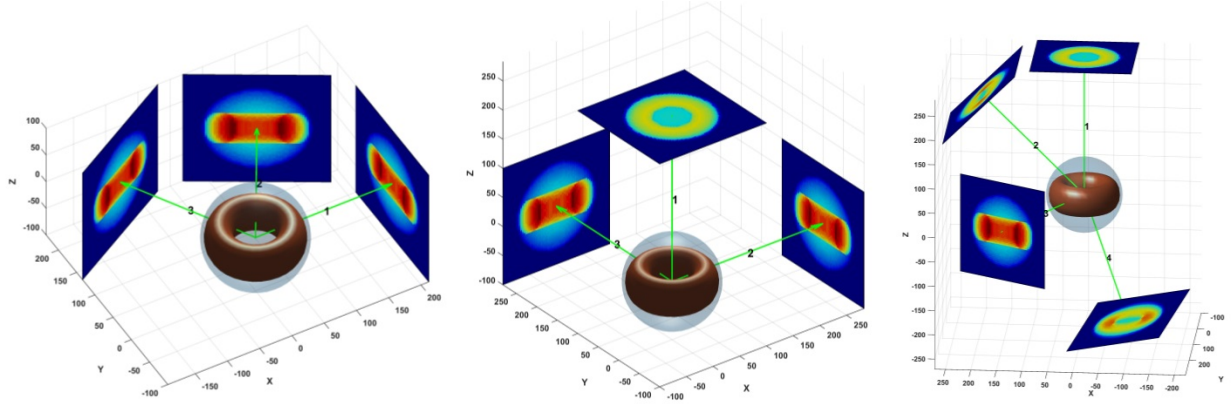

Figure 2. From left to right: a) three equatorial projections; b) three projections along coordinate axes; c) four projections more or less equally distributed over hemisphere. 2D projection positions are not to scale.

The source was reconstructed from the simulated projection data using the GEM algorithm with a quadratic potential ($p = 2$, see eq. (8)). The regularization parameter β was chosen so that $U(\mathbf{S})/\beta l(\mathbf{S}) \sim 10^{-3}$ at the end iteration. The volume grid consisted of $67 \times 67 \times 67$ voxels with voxel size $3 \times 3 \times 3$ micrometers cubed. The iteration was stopped when the relative change of residual norm became less than 10^{-4}. We choose to use this criterion to avoid the premature termination of iteration, taking into account that GEM algorithm is robust with respect to over iteration[9]. It should be noted that symmetry properties of the object were not used to improve the reconstruction. The same reconstruction parameters were used for all three projection schemes. The figures below illustrate the reconstruction results.
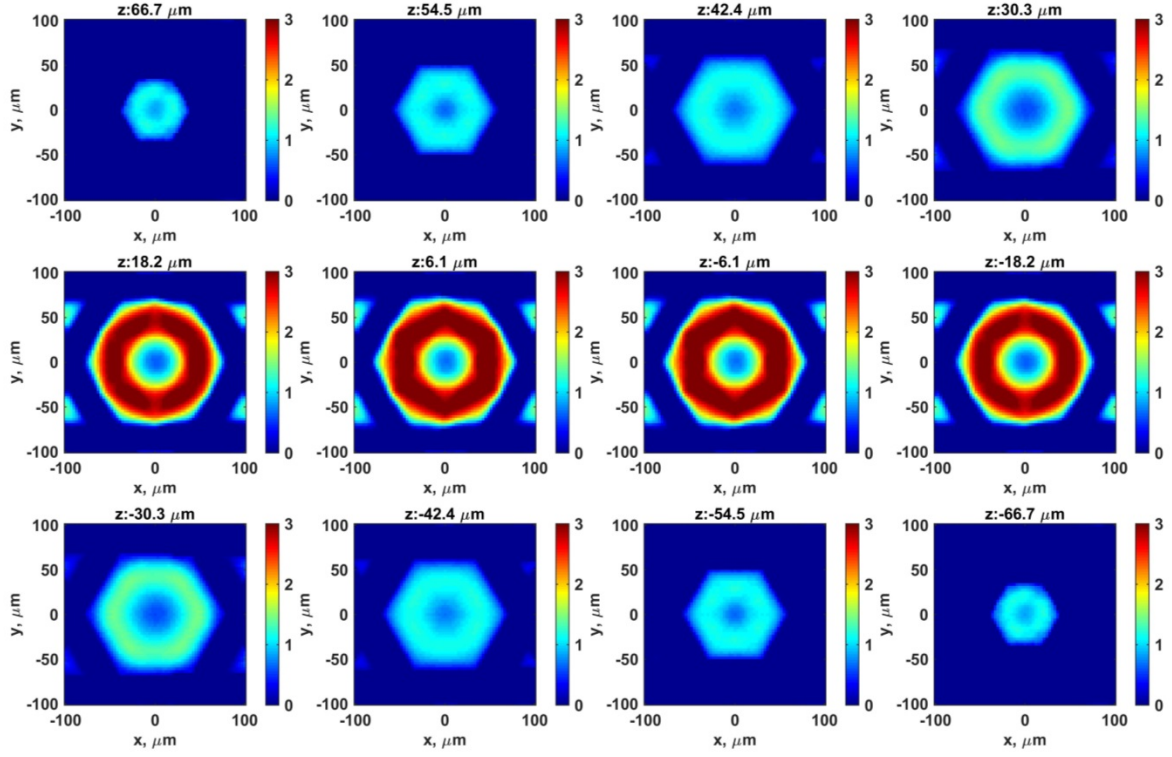
6

Figure 3. Reconstruction using three equatorial views (projection scheme a): *xy*-plane slices (every fourth slice is shown).

Figure 3 shows *xy*-plane slices of the 3D source reconstructed from three equatorial views (see Figure 2, projection scheme a). As it can be seen in this figure the reconstructed source preserves the main features of the original model source: i.e. a toroid with emission 3 a.u. inside a sphere with emission 1 a.u. However with only three equatorial views artifacts are introduced in the shape in directions that are not directly measured. The artifacts of the limited views results in a hexagonal structure, reflecting a six-fold rotation symmetry axis of projection directions, evident both in the shape of the toroid and in the shape of the sphere.
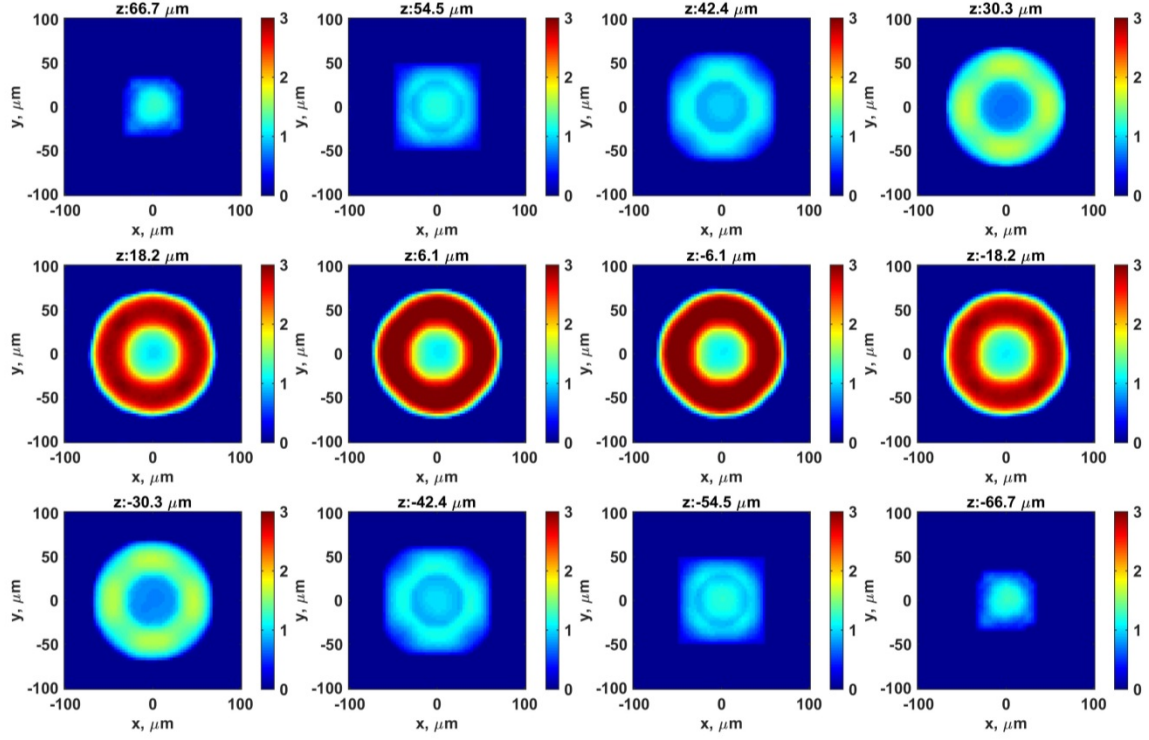
Figure 4. Three view along coordinate axes reconstruction (projection scheme b): *xy*-plane slices (every fourth slice is shown).

Figure 4 shows *xy*-plane slices of the 3D source reconstructed from three projections along the orthogonal coordinate axes (see Figure 2, projection scheme b). As it is evident from the figure, the shape of the reconstructed toroid exhibits rectangular artifacts consistent with the symmetry of the projection directions (three four-fold rotation axes); however, the artifacts in this case are not as pronounced as in the previous case. The polar areas of the reconstructed sphere show clear rectangular shape.
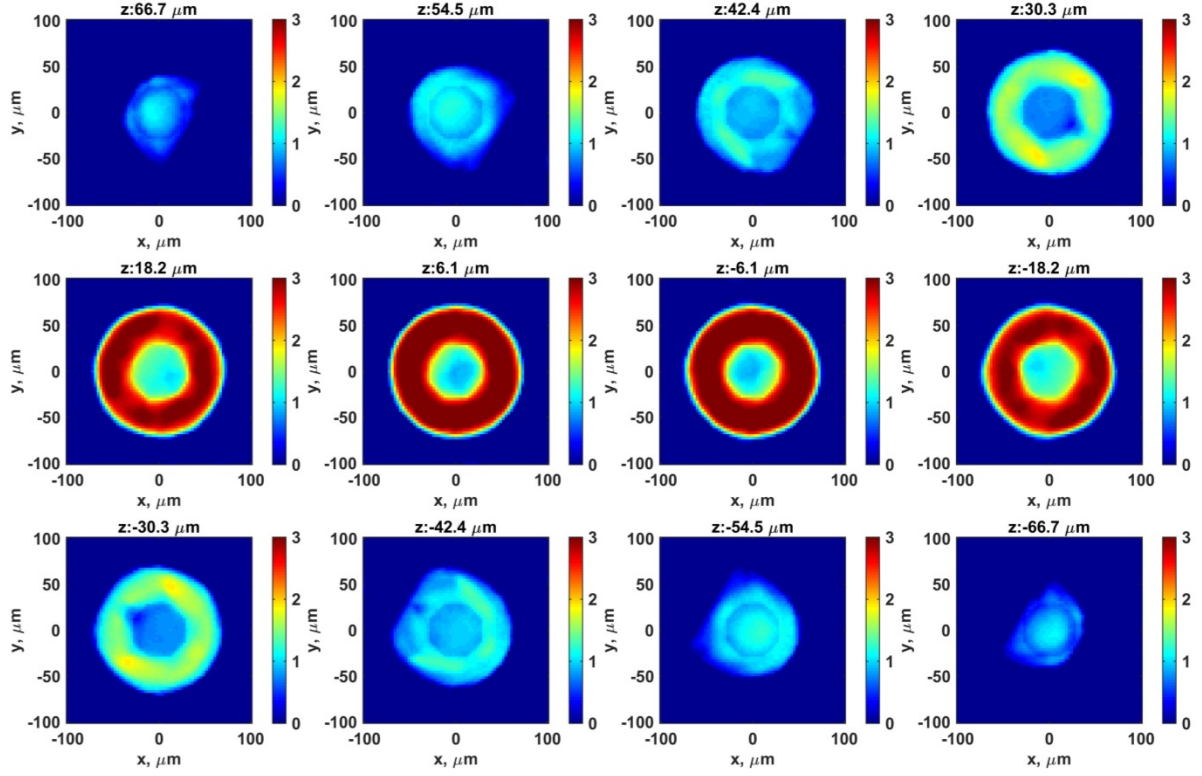
Figure 5. Four views reconstruction (projection scheme c): *xy*-plane slices (every fourth slice is shown).

Figure 5 shows *xy*-plane slices of the 3D source reconstructed from four projections more or less equally distributed over the hemisphere (see Figure 2, projection scheme c). In this case the projection directions do not have symmetry axes (a six-fold rotation axis for three equatorial views, and three four-fold rotation axes for the projections along coordinate axes). Consequently the artifacts in the reconstructed object do not exhibit the corresponding symmetry. But, once again, the reconstructed object exhibits artifacts due to inadequate sampling of the angular directions.

To further illustrate the shape of the reconstructed sources, the iso-surfaces of reconstructed objects are shown in Figure 6.
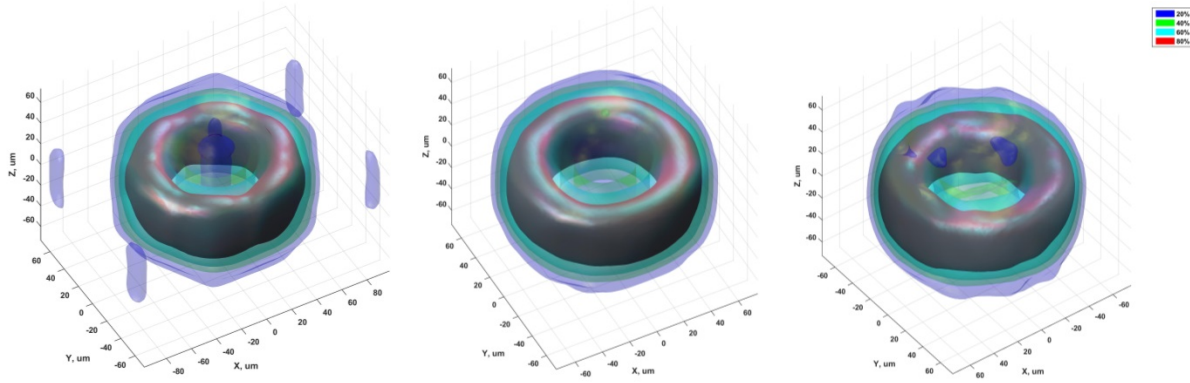
9

Figure 6. Iso-surface rendering of the reconstructed objects (from left to right): a) three equatorial projections; b) three projections along coordinate axis; c) four projections more or less equally distributed. The iso-surfaces are drawn at 20% (blue), 40% (green), 60% (cyan), and 80% (red) levels of maximum value of the reconstructed source.

As it is evident from Figure 2 in all three cases the main geometrical features on the model source are appropriately reconstructed. The reconstruction artifacts reflect the symmetry of the projection directions.

IV. EXPERIMENTAL DATA RECONSTRUCTION AND ANALYZYS

The algorithm was tested using multi-view x-ray imaging at the Omega Laser in Rochester, New York[19]. Four CID-based, time-integrated x-ray pinhole cameras recorded images of x-ray emission from deuterium filled capsule implosions, some of which were driven asymmetrically to produce oblate or prolate spheroid sources. These cameras were tuned to image the Bremsstrahlung emission from the hot core of the implosion, using 152 µm of Be and 203 µm Al filtration. Data from Omega shot #77186 was analyzed and is presented here.

The angles of the projections in the Omega coordinate system – (inclination, azimuth) in degrees – are as follows: 1–(37.8, 234.0), 2–(100.81, 54.0), 3–(100.81, 342.0), 4–(63.44, 54.0). To minimize the reconstruction volume the Omega coordinate system was rotated about an axis orthogonal both to the Omega drive axis and the *z*-axis to align the latter with the Omega drive axis. Figure 7 shows angular position of the views (projections) in this rotated coordinate system. The model object, described further in this section, is also shown in figure 7 to illustrate the symmetry and general shape of the x-ray source expected in this experiment.
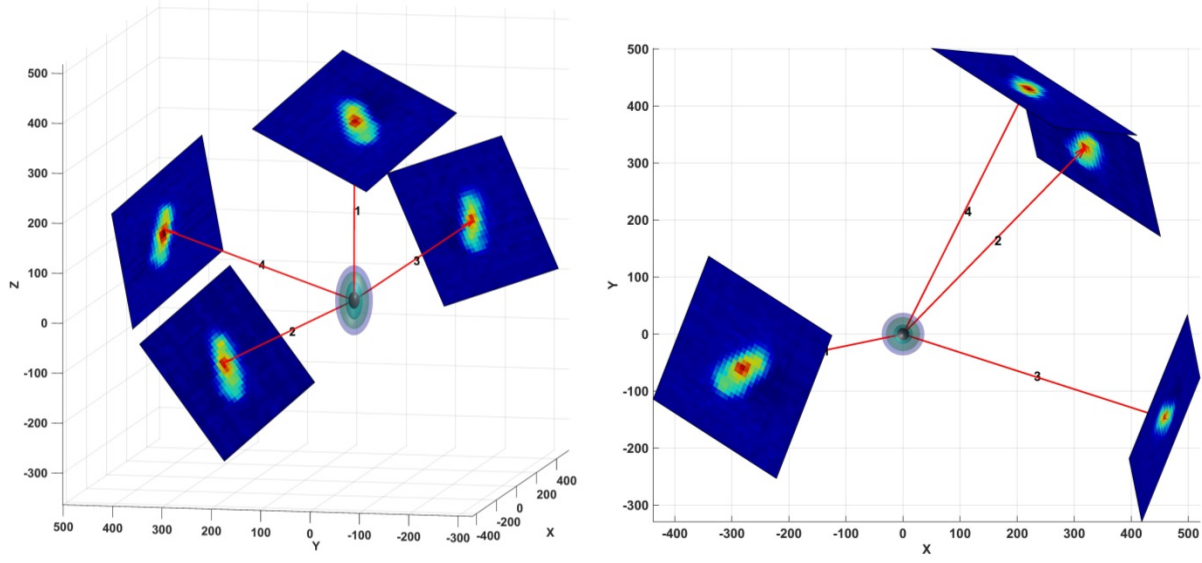
Figure 7. Projection directions in the coordinate system rotated to align Omega drive axis with the *z*-axis: equatorial view (left), and polar view (right). 2D projection positions are not to scale.

The 3D x-ray source was reconstructed using the GEM algorithm with a quadratic potential ($p = 2$, see eq. (8)). The regularization parameter β was chosen so that $U(\mathbf{S})/\beta l(\mathbf{S}) \sim 10^{-3}$ at the end iteration. The volume grid consisted of $21 \times 21 \times 21$ voxels with voxel size $9.6 \times 9.6 \times 9.6$ micrometers cubed. Iteration was stopped when the relative change of residual norm became less than 10^{-4}. The reconstruction results are shown in the figures below. Figure 8 shows *xy*-plane slices of the 3D source reconstructed from four projections and Figure 9 shows iso-surfaces drawn at different levels to illustrate the shape of the reconstructed source.
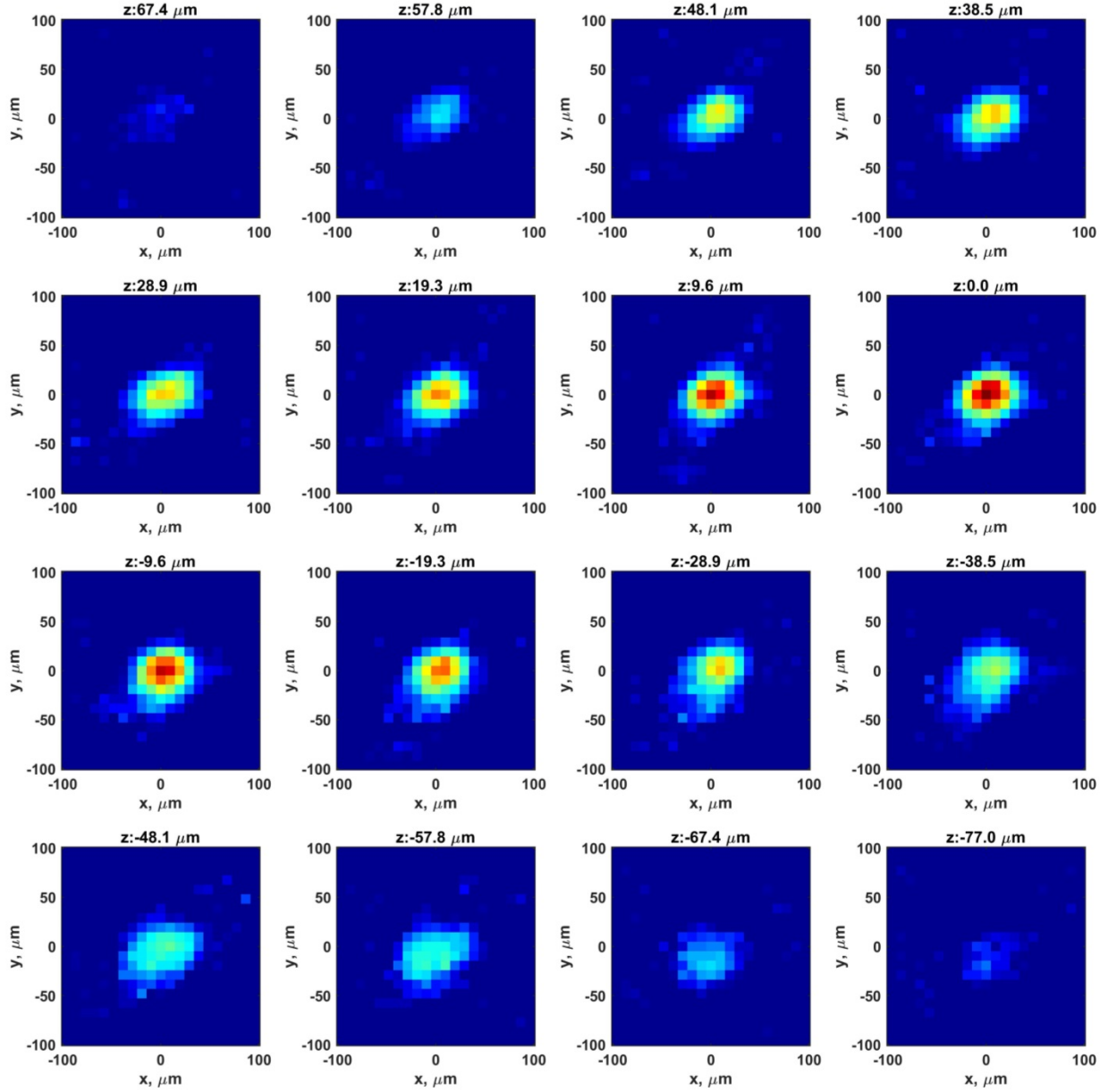
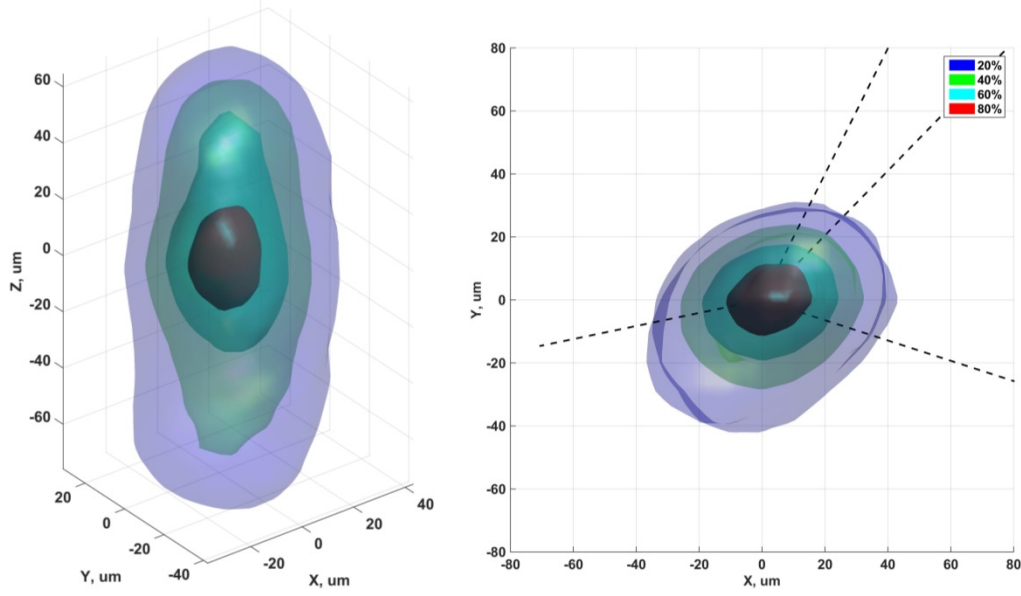Figure 8. Reconstructed 3D x-ray source: *xy*-plane slices

Figure 9. Iso-surfaces of the reconstructed 3D x-ray source from shot 77186: equatorial view (left), and polar view (right). The iso-surfaces are drawn at 20% (blue), 40% (green), 60% (cyan), and 80% (red) levels of maximum value of the reconstructed source. Black dashed lines in the polar view represent projection directions.

As is evident from Figure 8 and Figure 9 the shape and the size of the reconstructed source is close to what could be expected in this experiment. However, it is also evident from these figures, that the reconstructed object is somewhat elongated along the direction in equatorial plane, which the majority of the projection directions are roughly aligned. This might be due to the effect of overabundant projection directions studied in details in[20]. It has been shown[20] that some algorithms, such as ART or SIRT with the incorrect choice of reconstruction parameters, tend to elongate the reconstructed objects in the primary direction of projection (if the angular distribution of projection directions warrants a primary direction). One way to study the reconstruction results is to simulate the projection and the reconstruction of an object with the similar size and shape, but without noise. A comparison of the reconstructed results in simulation with the known initial source allows a study of the systematic errors in this reconstruction algorithm.

The model 3D source we used to study the reconstructed x-ray source consists of four prolate spheroids imbedded into each other. The major, minor semi-axes and the emission rates of the spheroids are selected so that the model source is close to the reconstructed x-ray source. The axes are: 1 – (70, 37.5), 2 – (57, 30), 3 – (38.5, 17), 4 – (17, 11). Here the numbers in parentheses are the major and minor semi-axes of the corresponding spheroids in micrometers. The emission rates of the spheroids are: 0.3, 0.5, 0.7, and 1 in arbitrary units. The model 3D x-ray source was reconstructed using the same algorithm and reconstruction parameters as were used to reconstruct the experimental x-ray source. Figure 10 shows iso-surfaces of the reconstructed model source.
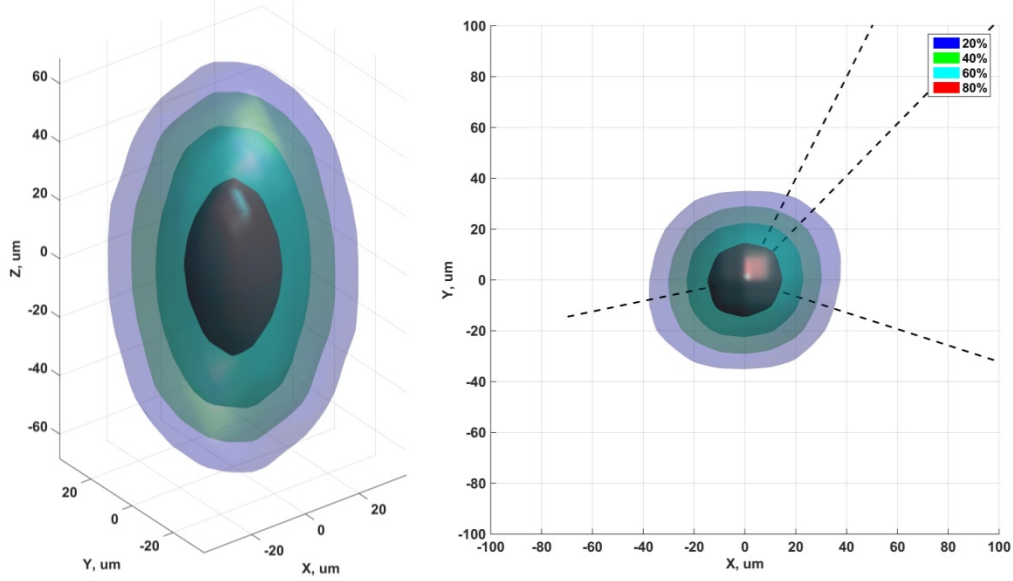
Figure 10. Iso-surfaces of the reconstructed model 3D x-ray source: equatorial view (left), and polar view (right). The iso-surfaces are drawn at 20% (blue), 40% (green), 60% (cyan), and 80% (red) levels of maximum value of the reconstructed source. Black dashed lines in the polar view represent projection directions.

As is evident from Figure 10 the reconstructed object has the correct overall shape and size, in addition the internal structure is also accurately reconstructed. The slight elongation along the primary direction of projection is visible in the right panel of Figure 10. However this elongation is rather small compared with the elongation of experimental source reconstruction. Thus, the analysis of the simulation results allows us to state, with high confidence, that the shape, the size, and the internal structure of the reconstructed x-ray source from the measured projections correctly describes the properties of the actual x-ray source.

V. CONCLUSIONS

As discussed earlier, to better understand the inherently three dimensional nature of ICF fusion implosions at NIF it is necessary to develop a multiple view neutron imaging technique that allows for the reconstruction of the three dimensional distribution of the hotspot and cold fuel. This requires the implementation of a tomographic imaging technique. One significant obstacle in developing and deploying such a system is that the number of views, which can be practically implemented, is limited to very few ~3. We conclude that the available experimental information from a few projections does not allow for reliable artifact free reconstruction of the three-dimensional source in the general case. However, as we have shown here, it is possible using an iterative EM algorithm with a Gibbs prior to reconstruct the three-dimensional source, which preserves the main features of the underlying source, using the two-dimensional projection data measured from only three directions. The reconstruction results faithfully measure the general shape (symmetry, topology), the size, and the internal structure of the three-dimensional object. The reconstructed distribution is not free from artifacts and is affected by projection symmetries and the angular distribution of projection directions. To minimize the artifacts, the projection directions should be judiciously

chosen. For the most accurate reconstruction of emission from nearly spherical ICF implosions the optimum projection directions are along three orthogonal axes. In order to avoid misinterpretation, such as attributing an artifact as features of a source, careful interpretation of the reconstructed result is needed. This can be done through simulation, where the projection and the reconstruction of a source with the similar size and shape is used to study and compare the simulated reconstruction artifacts with reconstructions from the experimental data.

VI. ACKNOWLEDGEMENTS

VII.   REFERENCES

1.   J. D. Lindl, O. L. Landen, J. Edwards, E. I. Moses, J. Adams, P. A. Amendt, N. Antipa, P. A. Arnold, L. J. Atherton, S. Azevedo, D. Barker, M. A. Barrios, I. Bass, S. H. Baxamusa, R. Beeler, B. V. Beeman, P. M. Bell, L. R. Benedetti, L. Bernstein, L. B. Hopkins, S. D. Bhandarkar, T. Biesiada, R. M. Bionta, D. L. Bleuel, E. J. Bond, M. Borden, M. W. Bowers, D. K. Bradley, D. Browning, G. K. Brunton, J. Bude, S. C. Burkhart, R. F. Burr, B. Butlin, J. A. Caggiano, D. A. Callahan, A. C. Carpenter, C. W. Carr, D. T. Casey, C. Castro, J. Celeste, P. M. Celliers, C. J. Cerjan, J. Chang, M. Chiarappa-Zucca, C. Choate, T. J. Clancy, D. S. Clark, S. J. Cohen, G. W. Collins, A. Conder, J. R. Cox, P. S. Datte, G. A. Deis, E. L. Dewald, P. Di Nicola, J. M. Di Nicola, L. Divol, S. N. Dixit, T. Doppner, V. Draggoo, O. Drury, R. Dylla-Spears, E. G. Dzenitis, J. M. Dzenitis, M. J. Eckart, D. C. Eder, J. H. Eggert, R. B. Ehrlich, G. V. Erbert, J. Fair, D. R. Farley, M. Fedorov, B. Felker, R. Finucane, A. Fisher, D. N. Fittinghoff, J. Folta, R. J. Fortner, T. Frazier, G. Frieders, S. Frieders, S. Friedrich, J. Fry, J. Gaylord, S. M. Glenn, S. H. Glenzer, B. Golick, G. Gururangan, G. Guss, S. W. Haan, B. J. Haid, B. Hammel, A. V. Hamza, E. P. Hartouni, R. Hatarik, B. W. Hatch, S. P. Hatchett, R. Hawley, C. Haynam, J. Heebner, G. Heestand, M. R. Hermann, V. J. Hernandez, D. G. Hicks, D. E. Hinkel, D. D. Ho, J. P. Holder, D. Holunga, J. Honig, J. Horner, R. K. House, M. Hutton, N. Izumi, M. C. Jackson, K. S. Jancaitis, D. R. Jedlovec, M. A. Johnson, O. S. Jones, D. H. Kalantar, R. L. Kauffman, L. Kegelmeyer, G. Kerbel, M. Key, S. F. Khan, J. R. Kimbrough, R. Kirkwood, J. J. Klingman, J. A. Koch, T. R. Kohut, J. M. Koning, K. M. Knittel, B. J. Kozioziemski, G. W. Krauter, K. Krauter, A. Kritcher, J. Kroll, W. L. Kruer, G. LaCaille, K. N. LaFortune, L. J. Lagin, T. A. Land, A. B. Langdon, S. H. Langer, D. W. Larson, D. A. Latray, T. Laurence, S. LePape, R. A. Lerche, Z. Liao, J. Liebman, R. A. London, R. R. Lowe-Webb, T. Ma, B. J.

MacGowan, A. J. MacKinnon, A. G. MacPhee, T. N. Malsbury, K. Manes, A. M. Manuel, E. R. Mapoles, M. M. Marinak, C. D. Marshall, D. Mason, N. Masters, D. G. Mathisen, I. Matthews, T. McCarville, J. M. McNaney, D. J. Meeker, N. B. Meezan, J. Menapace, P. Michel, P. E. Miller, J. L. Milovich, M. Mintz, R. Montesanti, M. Monticelli, J. D. Moody, M. J. Moran, J. C. Moreno, D. H. Munro, R. A. Negres, J. R. Nelson, M. Norton, M. Nostrand, M. O'Brien, Y. P. Opachich, C. Orth, A. E. Pak, E. S. Palma, J. N. E. Palmer, T. G. Parham, H. S. Park, P. K. Patel, R. W. Patterson, J. E. Peterson, J. L. Peterson, T. Phillips, R. Prasad, K. Primdahl, S. T. Prisbrey, S. R. Qiu, J. E. Ralph, K. S. Raman, F. Ravizza, B. Raymond, B. A. Remington, M. A. Rever, J. Reynolds, M. J. Richardson, A. C. Riddle, B. Rittmann, M. D. Rosen, J. S. Ross, J. R. Rygg, R. A. Sacks, J. T. Salmon, J. D. Salmonson, J. D. Sater, R. L. Saunders, R. Sawicki, K. Schaffers, D. H. Schneider, M. B. Schneider, H. A. Scott, S. M. Sepke, R. Seugling, D. A. Shaughnessy, M. J. Shaw, R. Shelton, N. Shen, N. Shingleton, N. Simanovskaia, V. Smalyuk, D. A. Smauley, M. Spaeth, B. K. Spears, D. R. Speck, T. M. Spinka, P. T. Springer, M. Stadermann, W. Stoeffl, J. Stolken, C. Stolz, E. Storm, D. J. Strozzi, T. Suratwala, L. J. Suter, J. S. Taylor, C. A. Thomas, G. L. Tietbohl, R. Tommasini, D. Trummer, B. VanWonterghem, R. Von Rotz, R. J. Wallace, C. F. Walters, A. Wang, A. L. Warrick, S. Weaver, S. V. Weber, P. J. Wegner, K. Widmann, C. C. Widmayer, E. A. Williams, P. K. Whitman, K. Wilhelmsen, M. Witte, L. Wong, R. D. Wood, S. Yang, C. Yeamans, B. K. Young, B. Yoxall, R. A. Zacharias, G. B. Zimmerman, S. Batha, C. R. Danly, V. Fatherley, G. P. Grim, N. Guler, H. W. Herrmann, Y. Kim, J. L. Kline, G. A. Kyrala, R. J. Leeper, D. Martinson, F. E. Merrill, R. E. Olson, C. Wilde, M. D. Wilke, D. C. Wilson, G. A. Chandler, G. W. Cooper, K. D. Hahn, K. J. Peterson, C. L. Ruiz, K. C. Chen, N. Dorsano, M. Emerich, C. Gibson, D. Hoover, M. Hoppe, J. D. Kilkenny, K. Moreno, H. Wilkens, S. Woods, J. A. Frenje, M. G. Johnson, C. K. Li, R. D. Petrasso, H. Rinderknecht, M. Rosenberg, F. H. Seguin, A. Zylstra, W. Garbett, P. Graham, T. Guymer, A. S. Moore, J. L. Bourgade, P. Gauthier, J. P. Leidinger, L. Masse, F. Philippe and R. H. H. Scott, Phys Plasmas **21** (12) (2014).

2.   S. H. Glenzer, D. A. Callahan, A. J. MacKinnon, J. L. Kline, G. Grim, E. T. Alger, R. L. Berger, L. A. Bernstein, R. Betti, D. L. Bleuel, T. R. Boehly, D. K. Bradley, S. C. Burkhart, R. Burr, J. A. Caggiano, C. Castro, D. T. Casey, C. Choate, D. S. Clark, P. Celliers, C. J. Cerjan, G. W. Collins, E. L. Dewald, P. DiNicola, J. M. DiNicola, L. Divol, S. Dixit, T. Doppner, R. Dylla-Spears, E. Dzenitis, M. Eckart, G. Erbert, D. Farley, J. Fair, D. Fittinghoff, M. Frank, L. J. A. Frenje, S. Friedrich, D. T. Casey, M. G. Johnson, C. Gibson, E. Giraldez, V. Glebov, S. Glenn, N. Guler, S. W. Haan, B. J. Haid, B. A. Hammel, A. V. Hamza, C. A. Haynam, G. M. Heestand, M. Hermann, H. W.

Hermann, D. G. Hicks, D. E. Hinkel, J. P. Holder, D. M. Holunda, J. B. Horner, W. W. Hsing, H. Huang, N. Izumi, M. Jackson, O. S. Jones, D. H. Kalantar, R. Kauffman, J. D. Kilkenny, R. K. Kirkwood, J. Klingmann, T. Kohut, J. P. Knauer, J. A. Koch, B. Kozioziemki, G. A. Kyrala, A. L. Kritcher, J. Kroll, K. La Fortune, L. Lagin, O. L. Landen, D. W. Larson, D. LaTray, R. J. Leeper, S. Le Pape, J. D. Lindl, R. Lowe-Webb, T. Ma, J. McNaney, A. G. MacPhee, T. N. Malsbury, E. Mapoles, C. D. Marshall, N. B. Meezan, F. Merrill, P. Michel, J. D. Moody, A. S. Moore, M. Moran, K. A. Moreno, D. H. Munro, B. R. Nathan, A. Nikroo, R. E. Olson, C. D. Orth, A. E. Pak, P. K. Patel, T. Parham, R. Petrasso, J. E. Ralph, H. Rinderknecht, S. P. Regan, H. F. Robey, J. S. Ross, M. D. Rosen, R. Sacks, J. D. Salmonson, R. Saunders, J. Sater, C. Sangster, M. B. Schneider, F. H. Seguin, M. J. Shaw, B. K. Spears, P. T. Springer, W. Stoeffl, L. J. Suter, C. A. Thomas, R. Tommasini, R. P. J. Town, C. Walters, S. Weaver, S. V. Weber, P. J. Wegner, P. K. Whitman, K. Widmann, C. C. Widmayer, C. H. Wilde, D. C. Wilson, B. Van Wonterghem, B. J. MacGowan, L. J. Atherton, M. J. Edwards and E. I. Moses, Phys Plasmas **19** (5) (2012).

3.   O. A. Hurricane, D. A. Callahan, D. T. Casey, P. M. Celliers, C. Cerjan, E. L. Dewald, T. R. Dittrich, T. Doppner, D. E. Hinkel, L. F. Berzak Hopkins, J. L. Kline, S. Le Pape, T. Ma, A. G. MacPhee, J. L. Milovich, A. Pak, H. S. Park, P. K. Patel, B. A. Remington, J. D. Salmonson, P. T. Springer and R. Tommasini, Nature **506** (7488), 343-348 (2014).

4.   S. W. Haan, J. D. Lindl, D. A. Callahan, D. S. Clark, J. D. Salmonson, B. A. Hammel, L. J. Atherton, R. C. Cook, M. J. Edwards, S. Glenzer, A. V. Hamza, S. P. Hatchett, M. C. Herrmann, D. E. Hinkel, D. D. Ho, H. Huang, O. S. Jones, J. Kline, G. Kyrala, O. L. Landen, B. J. MacGowan, M. M. Marinak, D. D. Meyerhofer, J. L. Milovich, K. A. Moreno, E. I. Moses, D. H. Munro, A. Nikroo, R. E. Olson, K. Peterson, S. M. Pollaine, J. E. Ralph, H. F. Robey, B. K. Spears, P. T. Springer, L. J. Suter, C. A. Thomas, R. P. Town, R. Vesey, S. V. Weber, H. L. Wilkens and D. C. Wilson, Phys Plasmas **18** (5) (2011).

5.   F. E. Merrill, D. Bower, R. Buckles, D. D. Clark, C. R. Danly, O. B. Drury, J. M. Dzenitis, V. E. Fatherley, D. N. Fittinghoff, R. Gallegos, G. P. Grim, N. Guler, E. N. Loomis, S. Lutz, R. M. Malone, D. D. Martinson, D. Mares, D. J. Morley, G. L. Morgan, J. A. Oertel, I. L. Tregillis, P. L. Volegov, P. B. Weiss, C. H. Wilde and D. C. Wilson, Rev Sci Instrum **83** (10) (2012).

6.   F. E. Merrill, K. S. Christensen, C. R. Danly, V. E. Fatherley, D. N. Fittinghoff, G. P. Grim, N. Izumi, D. R. Jedlovec, R. Hibbard, D. W. Schmidt, R. A. Simpson, K. Skulina, C. H. Wilde and P. L. Volegov, presented at the ICSF-2015, 404, 2015 (unpublished).

7. F. Natterer, *The Mathematics of Computerized Tomography*. (John Wiley&Sons, New York, 1986).

8. P. A. Penczek, Methods Enzymol. **482**, 1-33 (2010).

9. T. Hebert and L. Richard, IEEE Transactions on Medical Imaging **8** (2), 194-202 (1989).

10. P. Volegov, C. R. Danly, D. N. Fittinghoff, G. P. Grim, N. Guler, N. Izumi, T. Ma, F. E. Merrill, A. L. Warrick, C. H. Wilde and D. C. Wilson, Rev. Sci. Instrum. **85** (02358), 1-12 (2014).

11. R. Siddon, L., Med. Phys. **12** (2), 252-255 (1985).

12. L. A. Shepp and Y. Vardy, IEEE Transactions on Medical Imaging **MI-1** (2), 113-122 (1982).

13. L. B. Lucy, The Astronomical Journal **79** (6), 745-754 (1974).

14. W. H. Richardson, Journal of the Optical Society of America **62** (6), 55-59 (1972).

15. V. I. Gelfgat, E. L. Kosarev and E. R. Podulyak, Comp. Phys. Comm., 335-348 (1993).

16. S. Geman and D. E. McClure, Statistical Computational Section Proceedings of the American Statististical Association, 12-18 (1985).

17. R. Chartrand, Ieee T Signal Proces **60** (11), 5810-5819 (2012).

18. P. W. Lisowski and J. A. Paisner, presented at the Proceedings of the 4th International Topical Meeting on Nuclear Applications of Accelerator Technology, Washington, D.C., 2001 (unpublished).

19. T. R. Boehly, D. L. Brown, R. S. Craxton, R. L. Keck, J. P. Knauer, J. H. Kelly, T. J. Kessler, S. A. Kumpan, S. J. Loucks, S. A. Letzring, F. J. Marshall, R. L. McCrory, S. F. B. Morse, W. Seka, J. M. Soures and C. P. Verdon, Optics communications **133**, 495-506 (1997).

20. C. O. Sorzano, R. Marabini, N. Boisset, E. Rietzel, R. Schroder, G. T. Herman and J. M. Carazo, Journal of structural biology **133** (2-3), 108-118 (2001).